Research Square

Preprints are preliminary reports that have not undergone peer review.
They should not be considered conclusive, used to inform clinical practice,
or referenced by the media as validated information.

Moiré Artifact Reduction in Grating Interferometry Using Multiple Harmonics and Total Variation Regularization

Hunter M. Meyer
Louisiana State University
Joyoni Dey
deyj@lsu.edu

Louisiana State University
Conner B. Dooley
East Carolina University
Murtuza S. Taqi
Louisiana State University
Varun R. Gala
University of California, Santa Barbara
Christopher Morrison
Pennington Biomedical Research Center
Victoria L. Fontenot
Louisiana State University
Kyungmin Ham
Louisiana State University
Leslie G. Butler
Louisiana State University
Alexandra Noel
Louisiana State University

Article

Keywords:

Posted Date: November 7th, 2025

DOI: https://doi.org/10.21203/rs.3.rs-7776621/v1

License: This work is licensed under a Creative Commons Attribution 4.0 International License. Read Full License

Additional Declarations: Competing interest reported. JD, KH, and LGB are inventors of two patents related to the Modulated Phase Grating Interferometry. JD, HCM, and MST are inventors in a provisional patent related to X-ray interferometry, filed through Louisiana State University. All of the authors confirm that their work adheres to the ethical guidelines and standards for transparency and objectivity in conducting and reporting research.

Version of Record: A version of this preprint was published at Scientific Reports on April 14th, 2026. See the published version at https://doi.org/10.1038/s41598-026-48167-1.

Moiré Artifact Reduction in Grating Interferometry Using Multiple Harmonics and Total Variation Regularization

Hunter C. Meyer[1], Joyoni Dey[1,*], Conner B. Dooley[2], Murtuza S. Taqi[1], Varun R. Gala[3], Christopher Morrison[4], Victoria L. Fontenot[1], Kyungmin Ham[5], Leslie G. Butler[6], and Alexandra Noël[7]

[1]Department of Physics and Astronomy, Louisiana State University, Baton Rouge, LA 70803
[2]Department of Physics, East Carolina University, Greenville, NC 27858
[3]Department of Physics, University of California, Santa Barbara, CA 93106
[4]Pennington Biomedical Research Center, Baton Rouge, LA 70808
[5]Center for Advanced Microstructures and Devices, Louisiana State University, Baton Rouge, LA 70806
[6]Department of Chemistry, Louisiana State University, Baton Rouge, LA 70803
[7]Department of Comparative Biomedical Sciences, Louisiana State University School of Veterinary Medicine, Baton Rouge, LA 70803

[*]Corresponding Author: deyj@lsu.edu

Abstract

X-ray interferometry is an emerging imaging modality with a wide variety of potential clinical applications, including lung and breast imaging, as well as in non-destructive testing, such as additive manufacturing and porosimetry. A grating interferometer uses a diffraction grating to produce a periodic interference pattern and measures how a patient or sample perturbs the pattern, producing three unique images that highlight X-ray absorption, refraction, and small angle scattering, known as the attenuation, differential-phase, and dark-field images, respectively. Inaccuracies in grating position and multi-harmonic fringes produce Moiré artifacts when assuming the fringe pattern is perfectly sinusoidal and the phase steps are evenly spaced. We have developed an image recovery algorithm that estimates the true phase stepping positions using multiple harmonics and total variation regularization, removing the Moiré artifacts present in the attenuation, differential-phase, and dark-field images. We demonstrate the algorithm's utility for the Talbot-Lau and Modulated Phase Grating Interferometers by imaging multiple samples, including PMMA microspheres and a euthanized mouse.

1. Introduction

X-ray interferometry is a developing imaging modality with a wide variety of potential clinical and industrial applications. Of particular interest has been imaging lung disease, including emphysema [1], pulmonary fibrosis [2], COVID-19 [3], and cancer [4]. There have also been studies in breast imaging [5–8], where interferometric images have yielded higher contrast for microcalcifications. There has also been considerable interest in industrial applications and non-destructive testing, such as pore size analysis [9, 10] and additive manufacturing quality assurance [11, 12].

Grating interferometers are phase-sensitive imaging systems, measuring not only the absorption properties of the object or patient but also the phase properties, including refraction and small angle scattering [13, 14]. One or multiple diffraction gratings are placed between an X-ray source and detector, producing periodic fringe patterns. The object or patient perturbs the pattern, producing three unique images. X-ray absorption produces the attenuation image, calculated by measuring the change in the average value of the fringe pattern. This is the same as a traditional radiograph. X-ray refraction laterally shifts the fringe pattern, producing the differential-phase image, calculated by measuring the change in the phase of the fringe pattern. Small angle scattering reduces the fringe visibility — the height of the fringes relative to the average value — yielding the dark-field image. The strength of the differential-phase and dark-field signals depend on the system's phase sensitivity and autocorrelation length, respectively [15–18].

Grating interferometers commonly use a technique known as phase stepping to acquire images. The grating is translated laterally and imaged multiple times to produce a phase stepping curve at each pixel. Two phase stepping curves are acquired, one with no sample that serves as a reference curve and one with a sample in place, and the fringes are analyzed and compared on a per-pixel basis to simultaneously produce the three images. The phase stepping curves are typically assumed to be sinusoidal, and the average value, visibility, and phase are extracted and compared to produce the three images. Phase stepping requires the use of high precision electronic motors, since the phase steps are to the order of a micron, and at least five phase steps are usually acquired.

A key problem in grating interferometry is Moiré artifacts that result from small inaccuracies in grating position during the phase stepping procedure and the fact that the fringes are not perfectly sinusoidal. The artifacts appear as remnant oscillations in the measured average value, phase, and visibility of each pixel, ultimately leading to remnant oscillations in the attenuation, differential-phase, and dark-field images. Previous work on Moiré artifacts resulting from phase stepping errors and dose fluctuations has been reported [19–23]. However, these methods do not reduce the Moiré artifacts resulting from the influence of higher order harmonics present in the fringe patterns. As will be demonstrated, this is especially important for the Modulated Phase Grating Interferometer, though the influence of higher order harmonics may also prove useful for the Talbot-Lau Interferometer and Dual Phase Grating Interferometer.

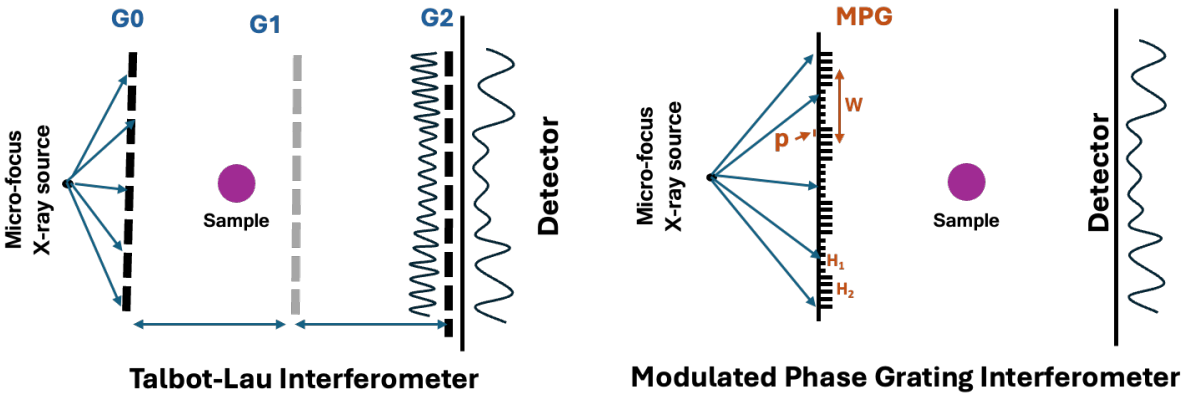
We propose the use of higher order harmonics to correct the phase step positions to remove the Moiré artifacts in the attenuation, differential-phase, and dark-field images. The phase step positions are estimated by minimizing the sum-squared error between the multi-harmonic model and measured data, as well as a regularization term, which is different for the reference and sample analysis. For the estimation of the reference phase stepping positions, the cost function is regularized by the total variation of the harmonic amplitudes. For the sample's phase stepping positions, the cost function is regularized by the total variation of the attenuation, differential-phase, and dark-field images. Higher order harmonic models for phase-shifting interferometry have been previously considered by Xu et al [24], but they only focused on the phase of the fringe pattern, as opposed to the average value or visibility, which are important for the attenuation and dark-field images. Additionally, our method of total variation regularization for estimating the phase stepping positions directly suppresses the Moiré artifacts in the attenuation, differential-phase, and dark-field images, which is important since the calculation of the attenuation and dark-field images *requires* the division of the sample and reference average value or visibility, respectively. Thus, without regularizing by the total variation of the calculated images, there could be minor residual Moiré artifacts in the raw parameters, which are then heightened in the calculated images.

2. Methods

2.1. Background

The Talbot-Lau Interferometer (TLI) is the most prevalent grating interferometry system that has been studied. There are three gratings, labeled G0, G1, and G2, shown in Figure 1a. The G1 grating is a phase grating that produces the fringe pattern. A typical X-ray tube's focal spot does not meet the coherence requirements necessary for high visibility fringes to form, so the G0 grating serves as a series of slits that are each small enough to produce fringes. The slits are evenly spaced at a period, p_0, so that the fringe pattern produced by each slit constructively interferes, allowing low brilliance sources to be used for interferometry [25]. The fringes produced by the G1 grating are smaller than typical detector pixels, so the G2 grating is used to serve as an analyzer. The period, p_2, is chosen to match the fringe period at the detector, p_D, so that a beat pattern is formed that is resolved by the detector.

The Modulated Phase Grating Interferometer (MPGI) is a recently developed X-ray system that is capable of interferometry without an analyzer grating [10, 26–29], shown in Figure 1b. The Modulated Phase Grating (MPG) is a diffraction grating that produces a periodic intensity pattern using either a microfocus source or standard X-ray source with a source grating, G0. The MPG has grating bars separated by a pitch, p, and the bar heights follow an envelope function with period, W. In the example shown, the envelope function is a RectMPG with phase-heights (H_1, H_2). The fringes produced by the MPG follow the magnified period of the envelope function, W, and the smaller pitch, p, determines the coherence requirements to be in accordance with other X-ray interferometers. Because W is fairly large, the fringes produced by the MPG are directly resolvable for standard high resolution X-ray detectors,



(a) TLI Schematic **(b)** MPGI Schematic

Figure 1. Schematics of the (a) Talbot-Lau and (b) Modulated Phase Grating Interferometers. In this study, the Talbot-Lau Interferometer used curved gratings. For the MPGI, a RectMPG was used and no G0 grating was used.

meaning no analyzer grating is required.

Attenuation, differential-phase, and dark-field images are calculated by acquiring two phase-stepping curves: a reference curve and a sample curve. A phase-stepping curve is a series of images generated by imaging the grating at several phase stepping positions, where the grating is laterally shifted over at least one period. The phase stepping curves are analyzed on a pixel-by-pixel basis by fitting the measured intensity to a sinusoidal function shown in Equation 1, where x_g is the phase stepping position, W is the period of the grating, and the fit parameters are a_0, a_1, and ϕ_1, representing the average value, amplitude, and phase of the fringe pattern, respectively. The subscript 1 represents that only one harmonic was used, and the superscripts represent distinct analysis for the reference, r, and sample, s. The fringe visibility is the ratio of the amplitude and average value, $V_1 = \frac{a_1}{a_0}$. The phase stepping positions are typically assumed to be evenly spaced and go over at least one period.

$$\hat{I}_1^{r,s}(x, y, x_g) = a_0^{r,s}(x, y) + a_1^{r,s}(x, y) \sin\left(\frac{2\pi x_g}{W} + \phi_1^{r,s}(x, y)\right) \tag{1}$$

The attenuation, differential-phase, and dark-field images are found by comparing each pixel's fit parameters between the reference and sample acquisitions, shown in Equations 2, 3, and 4.

$$\text{Attenuation} = \Gamma(x, y) = \frac{a_0^s}{a_0^r} \tag{2}$$

$$\text{Differential-phase} = \Delta\phi(x, y) = \phi_1^s - \phi_1^r \tag{3}$$

$$\text{Dark-field} = \Sigma(x, y) = \frac{V_1^s}{V_1^r} \tag{4}$$

The parameters are easily fit by forming a linear least squares problem by separating $\phi_1^{r,s}$ from the $\frac{2\pi x_g}{W}$ using the angle addition formula and minimizing the sum squared error of each pixel between the predicted intensity, $\hat{I}_1^{r,s}(x_g)$, and the measured intensity, $I_m^{r,s}(x_g)$ [30].

There are multiple assumptions used in the analysis. First, nominal values of x_g are typically used. That is to say, the phase steps are assumed to be evenly spaced. However, inaccuracies in grating position resulting from motor positional accuracy or system vibrations lead to remnant oscillations in the fit parameters found in Equation 1. Additionally, we assumed that the fringe pattern was perfectly sinusoidal, with only a single harmonic, but diffraction is highly complex, with many harmonics contributing to the produced interference pattern [10, 29]. Because we have a finite number of phase steps, the presence of multiple harmonics also leads to oscillations in the fitted visibility, even if the phase steps are truly evenly spaced. Since the oscillations in the fit parameters are not perfectly aligned between the sample and reference fringe patterns, there are substantial Moiré artifacts in the attenuation, differential-phase, and dark-field images, which appear as remnant grating fringes.

2.2. Iterative Phase Step Correction

In this work, we propose the use of a multi-harmonic model to estimate the true phase step positions, thereby reducing the Moiré artifacts. The phase step positions are estimated by iteratively minimizing a loss function that includes an error term and several regularization terms. Each iteration, the measured data is fit to the multi-harmonic model using that iteration's set of phase step positions, $\vec{\boldsymbol{x}}_{\boldsymbol{g}}$. The error term is the sum-squared error between the measured data and the model. The loss function includes a regularization term, R, and the optimization function is shown in Equation 5.

$$\hat{\boldsymbol{x}}_{\boldsymbol{g}} = \underset{\vec{\boldsymbol{x}}_{\boldsymbol{g}}}{\operatorname{argmin}} \sum_{x,y,x_g} \left(I_m(x,y,x_g) - \hat{I}(x,y,x_g) \right)^2 + R \tag{5}$$

Without regularization, estimating the true phase step positions only using the multi-harmonic model is an ill-posed problem. If the phase steps positions are incorrect, the higher order harmonics will be overfit to reduce the total sum-squared error, leading to a shallow local minima that is hard to escape. Additionally, the key parameters for interferometry images, a_0, a_1, and ϕ_1, will oscillate, which is what leads to the Moiré artifacts in the attenuation, differential-phase, and dark-field images. The goal of regularization is to penalize these oscillations, leading to phase step positions that yield attenuation, differential-phase, and dark-field images without Moiré artifacts.

The ill-posed nature of this problem is further overcome by first estimating the phase step positions using only the zeroth and first order harmonics. Then the phase step positions are estimated using up to the second harmonic, then up to the third. Each time a higher order harmonic is included, the upper and lower bounds are decreased. Equation 5 is minimized using the interior point algorithm, implemented via Matlab's *fmincon* function [31].

2.3. Multi-harmonic Model

Higher order harmonics are included in the intensity model, shown in Equation 6, where n_H is the maximum number of harmonics included in the model. The model is linearized using the sine angle addition theorem, shown in Equations 7–9.

$$\hat{I}^{r,s}(x,y,x_g) = a_0^{r,s}(x,y) + \sum_{n}^{n_H} a_n^{r,s}(x,y) \sin\left(\frac{2\pi n x_g}{W} + \phi_n^{r,s}(x,y) \right) \tag{6}$$

$$\hat{I}^{r,s}(x,y,x_g) = a_0^{r,s}(x,y) + \sum_{n}^{n_H} A_n^{r,s}(x,y) \sin\left(\frac{2\pi n x_g}{W} \right) + \sum_{n}^{n_H} B_n^{r,s}(x,y) \cos\left(\frac{2\pi n x_g}{W} \right) \tag{7}$$

$$A_n^{r,s}(x,y) = a_n^{r,s}(x,y) \cos\phi_n^{r,s}(x,y) \tag{8}$$

$$B_n^{r,s}(x,y) = a_n^{r,s}(x,y) \sin\phi_n^{r,s}(x,y) \tag{9}$$

Every iteration, linear least squares is performed using this iteration's set of phase step positions, $\vec{\boldsymbol{x}}_{\boldsymbol{g}}$. Similar to Marathe et al [30], a basis matrix is formed, $\boldsymbol{B}$, with matrix elements shown in Equation 10, where g denotes the phase step index and μ denotes the parameter index. The linear regression operator is calculated in Equation 11, and the parameters are estimated in Equation 12, where $\boldsymbol{I_m^{r,s}}\left(\vec{\boldsymbol{x}}_{\boldsymbol{g}}\right)$ is a column vector equal to this pixel's measured phase stepping curve.

$$B_{g\mu} = \begin{cases} 1 & \mu = 1 \\ \sin\left(\frac{2\pi(\mu/2)x_g}{W}\right) & \mu \text{ even} \\ \cos\left(\frac{2\pi((\mu-1)/2)x_g}{W}\right) & \mu \text{ odd, and } \mu \neq 1 \end{cases} \tag{10}$$

$$\boldsymbol{G} = \left(\boldsymbol{B}^T \cdot \boldsymbol{B}\right)^{-1} \cdot \boldsymbol{B}^T \tag{11}$$

$$\hat{\boldsymbol{A}}^{\boldsymbol{r,s}} = \boldsymbol{G} \cdot \boldsymbol{I_m^{r,s}}\left(\vec{\boldsymbol{x}}_{\boldsymbol{g}}\right) \tag{12}$$

The result, $\hat{\boldsymbol{A}}^{\boldsymbol{r,s}}$, is a column vector with $2n_H + 1$ entries that is transformed to calculate a_0, a_n, and ϕ_n, as shown in Equations 13–15.

$$a_0 = A_1 \tag{13}$$

$$a_n = \sqrt{A_{2n}^2 + A_{2n+1}^2} \tag{14}$$

$$\phi_n = \tan^{-1}\left(\frac{A_{2n+1}}{A_{2n}}\right) \tag{15}$$

There is a small implementation detail with the multi-harmonic model that is not shown in Equations 6–9. When calculating the differential-phase image, you have to subtract the phase of the first harmonic between the reference and sample data. Since the phase calculation results from an inverse tangent operation (Equation 15), this could lead to a phase wraparound artifact when the phase is near $\pm\pi$. To avoid this, the reference phase of each harmonic, $\phi_n^r(x, y)$ is included in the sine and cosine terms in the basis matrix elements when fitting the sample's phase stepping data. The differential-phase image, $\Delta\phi(x, y)$, is then calculated not by Equation 3, but as the phase of the first harmonic from Equation 15, avoiding the phase wraparound artifact by not required as subtraction of the reference phase.

2.4. Regularization

Regularization is included in the iterative estimation of the true phase step positions to avoid overfitting higher order harmonics that lead to oscillations in the fit parameters and remnant Moiré patterns in the attenuation, differential-phase, and dark-field images. Different regularization functions are chosen for the estimation of the phase step positions for the reference and sample acquisitions. Both cases require the use of the 2-dimensional anisotropic total variation (TV), shown in Equation 16, where f is some function of (x, y) and $\nabla_{x,y}$ represents the first derivative in the x or y direction.

$$TV\left(f(x, y)\right) = \sum_{x,y} |\nabla_x f(x, y)| + \sum_{x,y} |\nabla_y f(x, y)| \tag{16}$$

$$R^r = \sum_{n=0}^{n_H} \lambda_n TV\left(a_n(x, y)\right) \tag{17}$$

$$R^s = \lambda_\Gamma TV(\Gamma(x, y)) + \lambda_{\Delta\phi} TV(\Delta\phi(x, y)) + \lambda_\Sigma TV(\Sigma(x, y)) \tag{18}$$

For the reference acquisition, the regularization term used was the total variation of the magnitude of each harmonic, $a_n(x, y)$, including the zeroth harmonic. Each harmonic uses a different weighting factor, λ_n, as shown in Equation 17. This aims to reduce the oscillations in the individual fit parameters. However, we ultimately only care about the oscillations in the images, not the individual fit parameters. Because of this, the estimation of the sample's phase step positions was regularized by the TV of the three images: attenuation, $\Gamma(x, y)$, differential-phase, $\Delta\phi(x, y)$, and dark-field, $\Sigma(x, y)$. Each image was weighted by their own regularization factor, as shown in Equation 18.

2.5. Imaging Experiments

The proposed phase step correction method was evaluated by imaging multiple samples with a laboratory Talbot-Lau Interferometer (TLI) and Modulated Phase Grating Interferometer (MPGI). Both setups used the Hamamatsu L9181-02 microfocus X-ray source and Dexela 1512 X-ray detector with $75\,\mu m \times 75\,\mu m$ pixels.

The TLI setup consisted of three gratings, G0, G1, and G2, each with a period of $4.8\,\mu m$. The design energy was 31 keV. The G1 grating was a π-grating made of gold, with bar heights of $6.0\,\mu m$. The gratings were placed with a source-to-G0 distance of $5\,cm$, equal G0-to-G1 and G1-to-G2 distances of $43cm$, and a G2-to-detector distance of $3cm$. The source-to-sample distance was $32cm$. This corresponds to the symmetric geometry configuration described in Donath et al [18], with an autocorrelation length of $ACL = 3.58\,\mu m$. The gratings were curved to match the setup geometry. The microfocus X-ray tube was operated at 60 kVp, 70 μA, and under the large focal spot mode. Phase stepping was performed by stepping the G2 grating using a Newport VP-25XA motorized linear stage in $0.5\,\mu m$ increments, 10 second exposures, and 20 phase steps.

The MPGI setup used a RectMPG, with design heights of $(\pi/2, \pi/8)$ at $25\,keV$, a pitch of $p = 1\,\mu m$, and envelope period of $W = 120\,\mu m$. For more information, see MPG8 from Meyer et al [10]. A

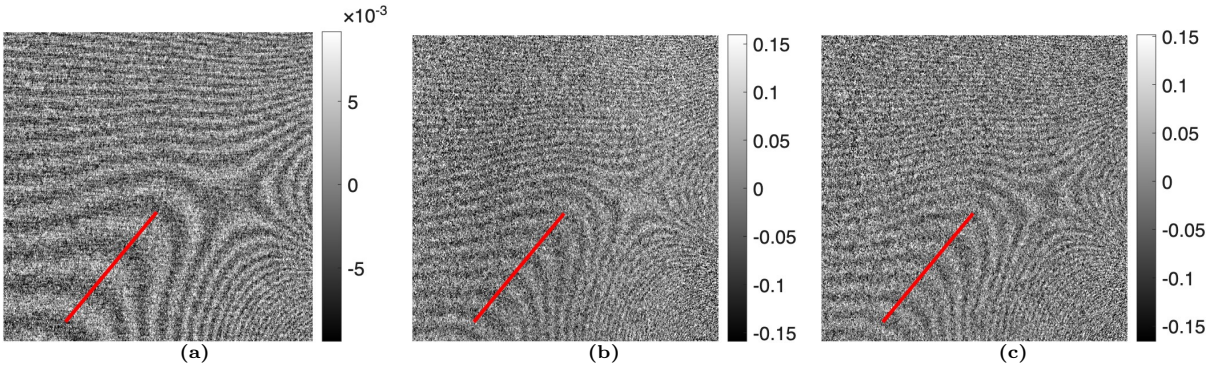


Figure 2. (a) Attenuation, (b) differential-phase, and (c) dark-field images taken with a TLI with no object (comparing two reference scans), calculated using the nominal phase steps. The amplitude of the Moiré artifact was calculated for the line of interest shown and statistically compared between the images calculated with the nominal phase steps and corrected phase steps.

source-to-detector distance of 110 cm is used, with a source-to-grating distance of 20 cm, yielding an autocorrelation length of $ACL = 67.64\,\mu m$. No G0 grating or G2 grating are used. Images were acquired at 45 kVp and 55 μA, under the small focal spot mode. Phase stepping was performed by stepping the MPG using a Newport AG-LS25-27P motorized linear stage with $12\mu m$ phase steps, 20 second exposures, and 10 phase steps.

The proposed algorithm's performance was evaluated in multiple ways. For the TLI setup, a "no object" case was tested by acquiring two phase stepping curves with no object in place, one serving as the "reference" and one serving as the "sample". This was done to evaluate the algorithm's ability to remove Moiré artifacts in the absence of a sample while still removing the grating inhomogeneities that are present in the parameter images (for instance $a_0(x, y)$ or $V(x, y)$). Additionally, a euthanized C57BL/6J (WT) mouse was imaged using the TLI. All animal-related procedures were approved by the Pennington Biomedical Research Center Institutional Animal Care and Use Committee (IACUC) and were carried out in strict adherence to the guidelines and regulations set by the NIH Office of Laboratory Animal Welfare. The mouse was euthanized via CO2 inhalation, transported to the imaging lab, mounted, and imaged by TLI. Using the MPGI, a sample of 1 μm PMMA microspheres was imaged.

3. Results

The proposed algorithm is first evaluated for the TLI setup. For the "no object" case, Moiré artifacts are clearly seen when the nominal phase step positions are used, as shown in Figure 2. The results of the proposed algorithm are shown in Figure 3, where it is clearly seen that the Moiré artifacts are almost completely removed. For the TLI setup, only 1 harmonic was needed. The regularization weights were $\lambda_\Gamma = 10^8$, $\lambda_{\Delta\phi} = 10^5$, and $\lambda_\Sigma = 10^5$. A line profile was taken through a region of the images with Moiré artifacts present. The line profiles were fit to a sinusoidal function, and the amplitude of the Moiré artifact was statistically compared between the images calculated using the nominal phase steps and corrected phase steps. It was found that the corrected phase steps produced images with significantly less ($\alpha = 0.05$) Moiré artifacts for all three images ($p < 0.001$ for all cases).

The algorithm was then tested on images of the euthanized mouse, shown in Figures 4 and 5. Once again, the Moiré artifacts are not visible when the proposed method is used. For the estimation of the phase step positions for the reference curve, the regularization weights chosen were $\lambda_n = 10^4$ for all n. For the sample phase steps, the regularization weights were $\lambda_\Gamma = 10^8$, $\lambda_{\Delta\phi} = 10^8$, and $\lambda_\Sigma = 10^8$. The order of magnitude of each weight was chosen so that the order of magnitude for the regularization term would be the same as the order of magnitude of the sum-squared error.

For the MPGI setup, a sample of 1 μm PMMA microspheres was imaged. The proposed algorithm was used with up to 3 harmonics, as opposed to only 1 harmonic for the TLI. Figure 6 compares the calculation of the average value, $a_0^r(x, y)$ calculated with the nominal phase steps and the corrected phase steps. It is seen that there is some residual Moiré artifacts when only 1 harmonic is used in the phase step correction algorithm. However, when 3 harmonics are used, it is seen that the Moiré artifacts are fully removed. This is even more noticeable for the comparison of the visibility seen in Figure 7. This translates to a complete removal of the Moiré artifacts in the attenuation, differential-phase, and dark-field images, as seen in Figures 8, 9, and 10. For the estimation of the phase stepping positions for

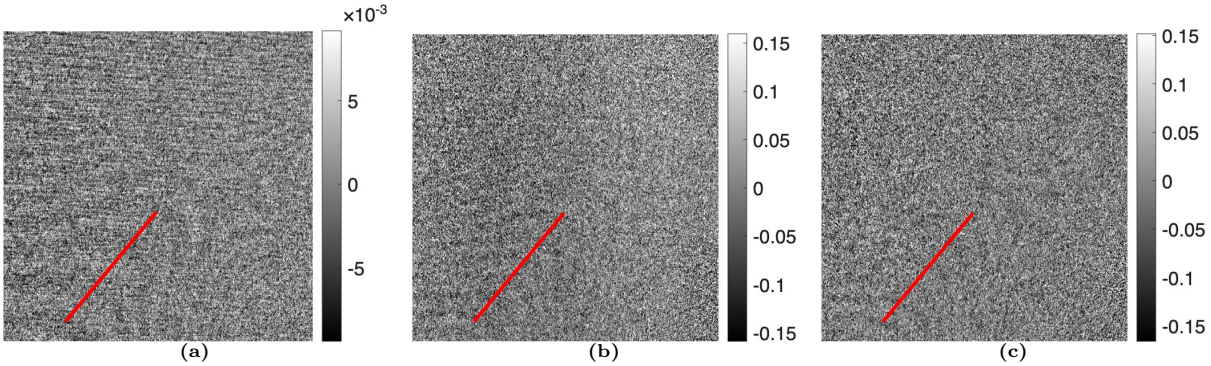


Figure 3. (a) Attenuation, (b) differential-phase, and (c) dark-field images taken with a TLI with no object (comparing two reference scans), calculated using the iterative method with 1 harmonic. The amplitude of the Moiré artifact was calculated for the line of interest shown and statistically compared between the images calculated with the nominal phase steps and corrected phase steps. It was found that the corrected phase steps produced images with significantly less ($\alpha = 0.05$) Moiré artifacts for all three images ($p < 0.001$ for attenuation, $p = 0.039$ for differential-phase, and $p = 0.005$ for dark-field).

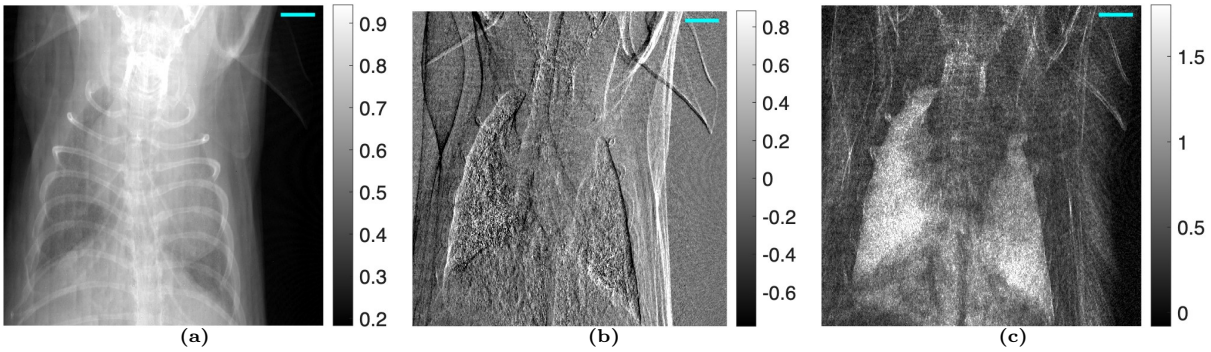


Figure 4. (a) Attenuation, (b) differential-phase, and (c) dark-field images taken with a TLI of a euthanized mouse, calculated using the nominal phase steps. A 3 mm scalebar is shown.

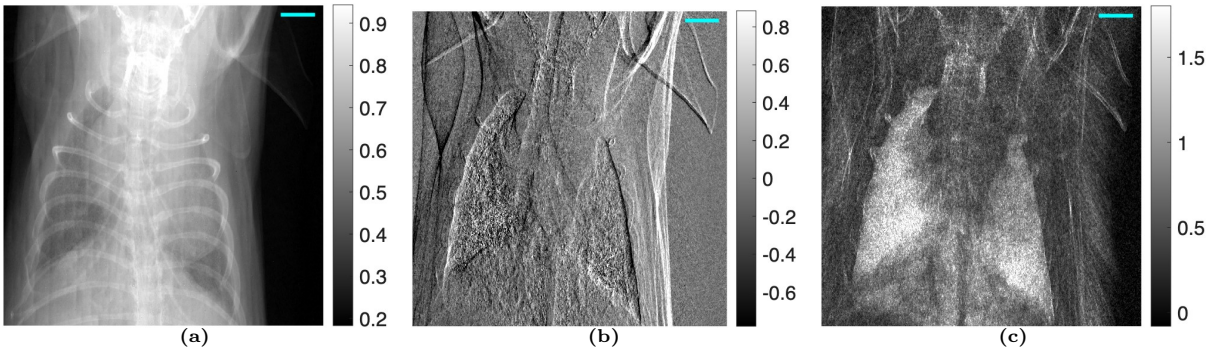


Figure 5. (a) Attenuation, (b) differential-phase, and (c) dark-field images taken with a TLI of a euthanized mouse, calculated using the iterative method with 1 harmonic. A 3 mm scalebar is shown.

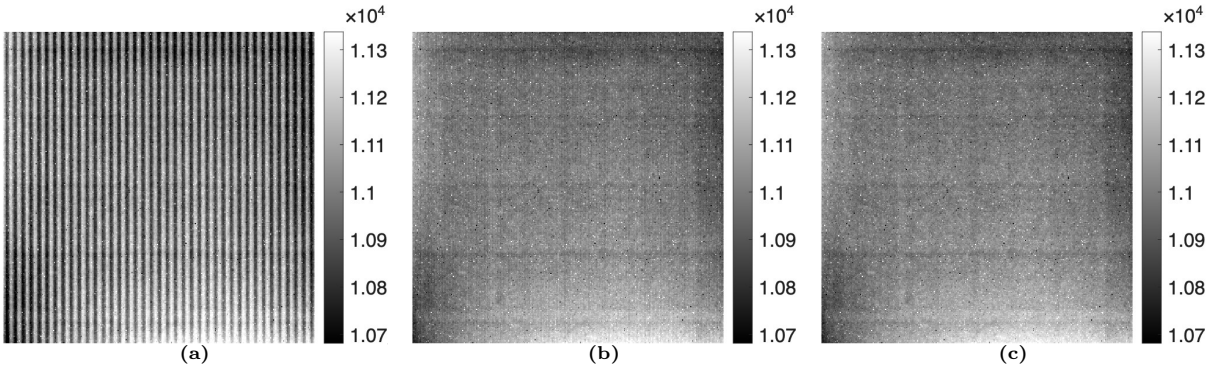


Figure 6. Comparison of the average value, $a_0^r(x, y)$, for the MPGI calculated with the (a) nominal phase steps, (b) phase steps estimated using the proposed method with 1 harmonic, and (c) phase steps using the proposed method with 3 harmonics.

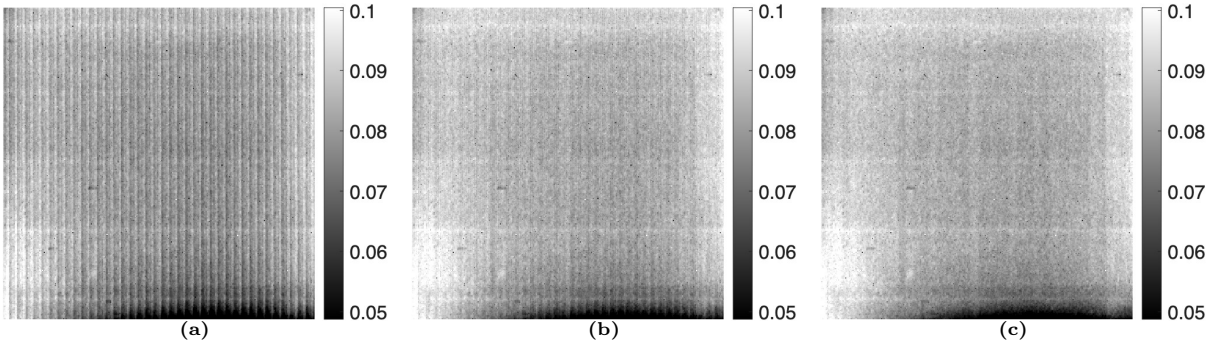


Figure 7. Comparison of the visibility, $V^r(x, y)$, for the MPGI calculated with (a) nominal phase steps, (b) corrected phase steps with 1 harmonic, and (c) corrected phase steps with 3 harmonics.

the reference curve, the regularization weights chosen were $\lambda_n = 10^4$ for all n. For the sample curve, the weights chosen were $\lambda_\Gamma = 10^{10}$, $\lambda_{\Delta\phi} = 10^9$, and $\lambda_\Sigma = 10^9$.

4. Discussion

We presented an iterative method for removing Moiré artifacts present in attenuation, differential-phase, and dark-field images by correcting phase step positions by modeling higher order harmonics in our phase stepping analysis. The methods were generally applicable to the Talbot-Lau Interferometer and Modulated Phase Grating Interferometer, and could easily be applied to the Dual Phase Grating Interferometer, where multiple harmonics are also observed [32]. While only 1 harmonic was necessary for the Talbot-Lau Interferometer in this instance, that will not be universally true, as it is possible to have more harmonic components for a Talbot-Lau Interferometer [33]. This shows that the methods presented are generally applicable to any phase-stepping grating interferometer, simply by an appropriate choice for the number of harmonics and regularization weights.

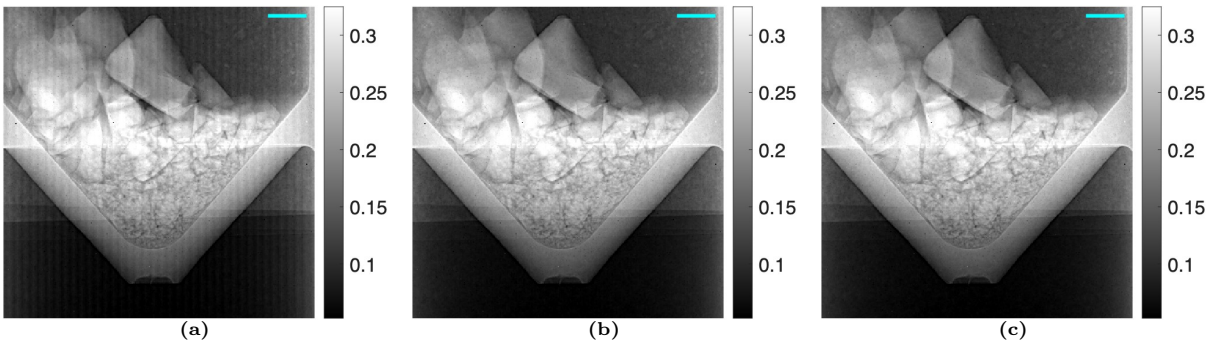


Figure 8. Comparison of the attenuation image, $\Gamma(x, y)$, for the MPGI calculated with (a) nominal phase steps, (b) corrected phase steps with 1 harmonic, and (c) corrected phase steps with 3 harmonics. A 1 mm scalebar is shown.

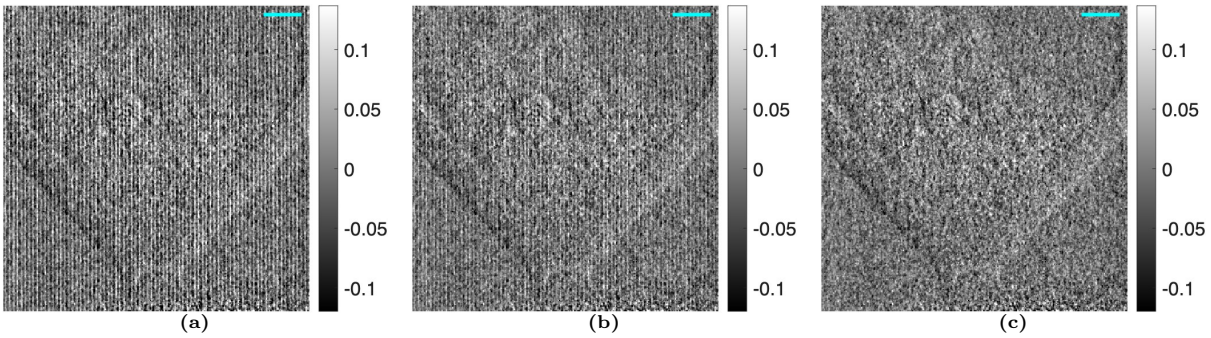


Figure 9. Comparison of the differential-phase image, $\Delta\phi(x, y)$, for the MPGI calculated with (a) nominal phase steps, (b) corrected phase steps with 1 harmonic, and (c) corrected phase steps with 3 harmonics. A 1 mm scalebar is shown.

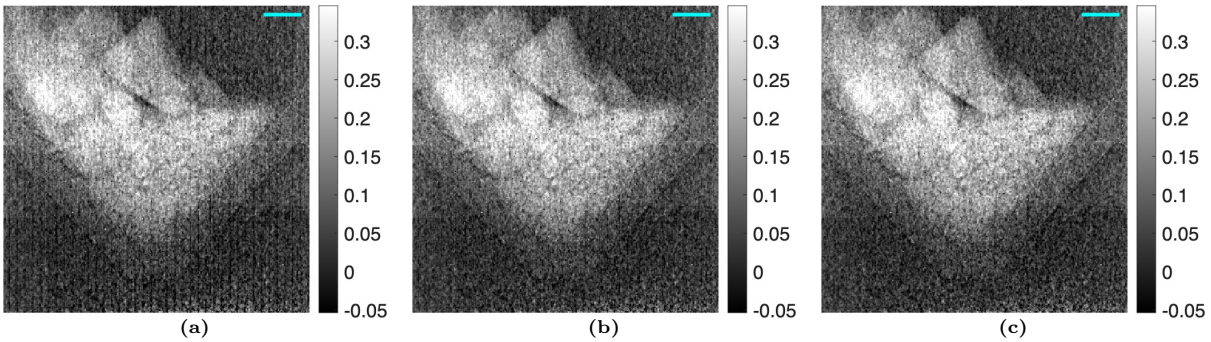


Figure 10. Comparison of the dark-field image, $\Sigma(x, y)$, for the MPGI calculated with (a) nominal phase steps, (b) corrected phase steps with 1 harmonic, and (c) corrected phase steps with 3 harmonics. A 1 mm scalebar is shown.

The methods presented reduced or completely eliminated the image artifacts in all three images for multiple samples and multiple interferometers, highlighting the robustness of the image recovery algorithm. The methods even worked when there was extreme curvature of the fringes in the Talbot-Lau Interferometer, resulting from misalignment of the curved gratings. Additionally, our method works by analyzing the TV of the entire image, not just a subregion. While the previous literature has also focused on dose fluctuations, our setup used a microfocus X-ray source with long exposures, so this was not necessary in our analysis. However, it would be relatively straightforward to implement such a correction.

The robust artifact removal represents a significant step not only for visualizing but also for quantitatively characterizing diseases of the lungs (including emphysema, fibrosis, and cancer), as well as potentially other applications such as osteoporosis, breast cancer imaging, quantitative imaging of porosity in different objects, and quality assessment of additive manufacturing.

With the introduction of a multi-harmonic analysis, there is the potential to isolate higher harmonic dark-field images and analyze them separately from the first harmonic image. While this analysis is not possible in our case due to the strength and signal-to-noise ratio of each harmonic, this may prove useful for simultaneous imaging of multiple autocorrelation lengths, so long as the visibility of each harmonic is high enough.

5. Conclusions

X-ray interferometry has the potential for a wide variety of clinical and industrial applications, but unique image artifacts are introduced when assuming the phase stepping positions are evenly spaced and that the phase stepping curves are perfectly sinusoidal. By including higher order harmonics and utilizing total variation regularization in our analysis, we have significantly reduced Moiré artifacts in attenuation, differential-phase, and dark-field images taken with a Talbot-Lau Interferometer and Modulated Phase Grating Interferometer.

6. Acknowledgments

This work is funded in part by NIH NIBIB Trail-blazer Award 1-R21-EB029026-01A1. The authors thank the Inhalation Research Facility of the School of Veterinary Medicine Louisiana State University, for technical support. We also thank the National Science Foundation for the support of CBD through the REU site at Louisiana State University in the Department of Physics and Astronomy (NSF Grant No. 2150445). This research was supported in part by the Dr. Charles M. Smith Jr. Superior Graduate Student Scholarship in Medical Physics at the Louisiana State University-Mary Bird Perkins Cancer Center Medical Physics Program. We also thank the Louisiana State University Charles E. Coates Memorial Fund for support.

7. Author Contributions

HCM developed and implemented the algorithms, applied them to the datasets, prepared manuscript, and assisted in supervising CBD, VRG, and VLF. JD provided overall supervision and contributed to all aspects of this project. CBD contributed to the development and analysis of multi-harmonic corrections. MST helped with mouse experiments. VRG helped in statistical analysis. CM provided the mouse sample. VLF helped with the phase-step corrections. KH and LGB helped setup the X-ray system. AN provided pre-experiment samples to optimize the system. All authors reviewed the manuscript.

8. Funding

JD and HCM were funded in part by NIH NIBIB Trail-blazer Award 1-R21-EB029026-01A1. HCM was also supported in part by the Dr. Charles M. Smith Jr. Superior Graduate Student Scholarship in Medical Physics at the Louisiana State University-Mary Bird Perkins Cancer Center Medical Physics Program. CBD was supported by the National Science Foundation through the REU site at Louisiana State University in the Department of Physics and Astronomy (NSF Grant No. 2150445)

9. Data Availability

The datasets analyzed during the current study are available in the GitHub repository, https://github.com/huntercmeyer/artifact_project_repository or from the corresponding author upon reasonable request.

10. Competing Interests

JD, KH, and LGB are inventors of two patents related to the Modulated Phase Grating Interferometry [26, 27]. JD, HCM, and MST are inventors in a provisional patent related to X-ray interferometry, filed through Louisiana State University. All of the authors confirm that their work adheres to the ethical guidelines and standards for transparency and objectivity in conducting and reporting research.

References

[1] Theresa Urban, Florian T. Gassert, Manuela Frank, et al. "Dark-field chest radiography signal characteristics in inspiration and expiration in healthy and emphysematous subjects". In: *European Radiology Experimental* 9.1 (Mar. 2025), p. 40. ISSN: 2509-9280. DOI: 10.1186/s41747-025-00578-x. URL: https://doi.org/10.1186/s41747-025-00578-x.

[2] Katharina Hellbach, Andre Yaroshenko, Konstantin Willer, et al. "X-ray dark-field radiography facilitates the diagnosis of pulmonary fibrosis in a mouse model". In: *Scientific Reports* 7.1 (Mar. 2017), p. 340. ISSN: 2045-2322. DOI: 10.1038/s41598-017-00475-3. URL: https://doi.org/10.1038/s41598-017-00475-3.

[3] Florian T. Gassert, Henriette Bast, Theresa Urban, et al. "Comparison of dark-field chest radiography and CT for the assessment of COVID-19 pneumonia". In: *Frontiers in Radiology* Volume 4 - 2024 (2025). ISSN: 2673-8740. DOI: 10.3389/fradi.2024.1487895. URL: https://www.frontiersin.org/journals/radiology/articles/10.3389/fradi.2024.1487895.

[4] Kai Scherer, Andre Yaroshenko, Deniz Ali Bölükbas, et al. "X-ray Dark-field Radiography - In-Vivo Diagnosis of Lung Cancer in Mice". In: *Scientific Reports* 7.1 (Mar. 2017), p. 402. ISSN: 2045-2322. DOI: 10.1038/s41598-017-00489-x. URL: https://doi.org/10.1038/s41598-017-00489-x.

[5] Zhentian Wang, Nik Hauser, Gad Singer, et al. "Non-invasive classification of microcalcifications with phase-contrast X-ray mammography". In: *Nature Communications* 5.1 (May 2014), p. 3797. ISSN: 2041-1723. DOI: 10.1038/ncomms4797. URL: https://doi.org/10.1038/ncomms4797.

[6] Kai Scherer, Lorenz Birnbacher, Michael Chabior, et al. "Bi-Directional X-Ray Phase-Contrast Mammography". In: *PLOS ONE* 9.5 (May 2014), pp. 1–7. DOI: 10.1371/journal.pone.0093502. URL: https://doi.org/10.1371/journal.pone.0093502.

[7] Thomas Koehler, Heiner Daerr, Gerhard Martens, et al. "Slit-scanning differential x-ray phase-contrast mammography: proof-of-concept experimental studies". en. In: *Med Phys* 42.4 (Apr. 2015), pp. 1959–1965.

[8] Arne Tapfer, Martin Bech, Astrid Velroyen, et al. "Experimental results from a preclinical X-ray phase-contrast CT scanner". en. In: *Proc Natl Acad Sci U S A* 109.39 (Sept. 2012), pp. 15691–15696.

[9] V. Revol, I. Jerjen, C. Kottler, et al. "Sub-pixel porosity revealed by x-ray scatter dark field imaging". In: *Journal of Applied Physics* 110.4 (Aug. 2011), p. 044912. ISSN: 0021-8979. DOI: 10.1063/1.3624592. eprint: https://pubs.aip.org/aip/jap/article-pdf/doi/10.1063/1.3624592/13589811/044912_1_online.pdf. URL: https://doi.org/10.1063/1.3624592.

[10] Hunter Meyer, Joyoni Dey, Sydney Carr, et al. "Theoretical and experimental analysis of the modulated phase grating X-ray interferometer". In: *Scientific Reports* 14.1 (Nov. 2024), p. 26780.

[11] Xiayun Zhao and David W. Rosen. "Real-time interferometric monitoring and measuring of photopolymerization based stereolithographic additive manufacturing process: sensor model and algorithm". In: *Measurement Science and Technology* 28 (2016). URL: https://api.semanticscholar.org/CorpusID:125660749.

[12] Adam J. Brooks, Hong Yao, Jumao Yuan, et al. "Early detection of fracture failure in SLM AM tension testing with Talbot-Lau neutron interferometry". In: *Additive Manufacturing* 22 (2018), pp. 658–664. ISSN: 2214-8604. DOI: https://doi.org/10.1016/j.addma.2018.06.012. URL: https://www.sciencedirect.com/science/article/pii/S221486041730324X.

[13] Atsushi Momose. "Recent Advances in X-ray Phase Imaging". In: *Japanese Journal of Applied Physics* 44.9R (Sept. 2005), p. 6355. DOI: 10.1143/JJAP.44.6355. URL: https://dx.doi.org/10.1143/JJAP.44.6355.

[14] F. Pfeiffer, M. Bech, O. Bunk, et al. "X-ray dark-field and phase-contrast imaging using a grating interferometer". In: *Journal of Applied Physics* 105.10 (May 2009), p. 102006. ISSN: 0021-8979. DOI: 10.1063/1.3115639. eprint: https://pubs.aip.org/aip/jap/article-pdf/doi/10.1063/1.3115639/15038269/102006_1_online.pdf. URL: https://doi.org/10.1063/1.3115639.

[15] W. Yashiro, Y. Terui, K. Kawabata, et al. "On the origin of visibility contrast in x-ray Talbot interferometry". In: *Opt. Express* 18.16 (Aug. 2010), pp. 16890–16901. DOI: 10.1364/OE.18.016890. URL: https://opg.optica.org/oe/abstract.cfm?URI=oe-18-16-16890.

[16] M. Strobl. "General solution for quantitative dark-field contrast imaging with grating interferometers". In: *Scientific Reports* 4.1 (Nov. 2014), p. 7243. ISSN: 2045-2322. DOI: 10.1038/srep07243. URL: https://doi.org/10.1038/srep07243.

[17] Spyridon Gkoumas, Pablo Villanueva-Perez, Zhentian Wang, et al. "A generalized quantitative interpretation of dark-field contrast for highly concentrated microsphere suspensions". In: *Scientific Reports* 6.1 (Oct. 2016), p. 35259. ISSN: 2045-2322. DOI: 10.1038/srep35259. URL: https://doi.org/10.1038/srep35259.

[18] Tilman Donath, Michael Chabior, Franz Pfeiffer, et al. "Inverse geometry for grating-based x-ray phase-contrast imaging". In: *Journal of Applied Physics* 106.5 (Sept. 2009), p. 054703. ISSN: 0021-8979. DOI: 10.1063/1.3208052. eprint: https://pubs.aip.org/aip/jap/article-pdf/doi/10.1063/1.3208052/14797839/054703_1_online.pdf. URL: https://doi.org/10.1063/1.3208052.

[19] Sebastian Kaeppler, Jens Rieger, Georg Pelzer, et al. "Improved reconstruction of phase-stepping data for Talbot–Lau x-ray imaging". In: *Journal of Medical Imaging* 4.3 (2017), p. 034005. DOI: 10.1117/1.JMI.4.3.034005. URL: https://doi.org/10.1117/1.JMI.4.3.034005.

[20] Christian Hauke, Martino Leghissa, Georg Pelzer, et al. "Analytical and simulative investigations of moiré artefacts in Talbot-Lau X-ray imaging". In: *Opt. Express* 25.26 (Dec. 2017), pp. 32897–32909. DOI: 10.1364/OE.25.032897. URL: https://opg.optica.org/oe/abstract.cfm?URI=oe-25-26-32897.

[21] Koh Hashimoto, Hidekazu Takano, and Atsuhi Momose. "Improved reconstruction method for phase stepping data with stepping errors and dose fluctuations". In: *Opt. Express* 28.11 (May 2020), pp. 16363–16384. DOI: 10.1364/OE.385236. URL: https://opg.optica.org/oe/abstract.cfm?URI=oe-28-11-16363.

[22] Siwei Tao, Yueshu Xu, Ling Bai, et al. "Moiré artifacts reduction in Talbot-Lau X-ray phase contrast imaging using a three-step iterative approach". In: *Opt. Express* 30.20 (Sept. 2022), pp. 35096–35111. DOI: 10.1364/OE.466277. URL: https://opg.optica.org/oe/abstract.cfm?URI=oe-30-20-35096.

[23] Ohsung Oh, Daeseung Kim, Ho Kyung Kim, et al. "Image reconstruction method in grating interferometer with phase stepping using grating position and dose fluctuation correction". In: *Journal of Instrumentation* 18.07 (July 2023), P07006. DOI: 10.1088/1748-0221/18/07/P07006. URL: https://dx.doi.org/10.1088/1748-0221/18/07/P07006.

[24] Jiancheng Xu, Qiao Xu, and Liqun Chai. "An iterative algorithm for interferograms with random phase shifts and high-order harmonics". In: *Journal of Optics A: Pure and Applied Optics* 10.9 (Aug. 2008), p. 095004. DOI: 10.1088/1464-4258/10/9/095004. URL: https://dx.doi.org/10.1088/1464-4258/10/9/095004.

[25] Franz Pfeiffer, Timm Weitkamp, Oliver Bunk, et al. "Phase retrieval and differential phase-contrast imaging with low-brilliance X-ray sources". In: *Nature Physics* 2.4 (Apr. 2006), pp. 258–261. ISSN: 1745-2481. DOI: 10.1038/nphys265. URL: https://doi.org/10.1038/nphys265.

[26] J. Dey, N. Bhusal, L. Butler, et al. *Phase Contrast X-ray Interferometry*. US Patent 10,872,708, Dec 22, 2020.

[27] J. Dey, N. Bhusal, L. Butler, et al. *Phase Contrast X-ray Interferometry*. US Patent 11,488,740 B2, Nov 1, 2022.

[28] Jingzhu Xu, Kyungmin Ham, and Joyoni Dey. "X-ray interferometry without analyzer for breast CT application: a simulation study". In: *Journal of Medical Imaging* 7.2 (2020), p. 023503. DOI: 10.1117/1.JMI.7.2.023503. URL: https://doi.org/10.1117/1.JMI.7.2.023503.

[29] I. Hidrovo, J. Dey, H. Meyer, et al. "Neutron interferometry using a single modulated phase grating". In: *Review of Scientific Instruments* 94.4 (Apr. 2023), p. 045110.

[30] S. Marathe, L. Assoufid, X. Xiao, et al. "Improved algorithm for processing grating-based phase contrast interferometry image sets". In: *Rev Sci Instrum* 85.1 (Jan. 2014), p. 013704.

[31] The MathWorks Inc. *Optimization Toolbox version: 25.1 (R2025a)*. Natick, Massachusetts, United States, 2025. URL: https://www.mathworks.com.

[32] Aimin Yan, Xizeng Wu, and Hong Liu. "Clarification on generalized Lau condition for X-ray interferometers based on dual phase gratings". In: *Opt. Express* 27.16 (Aug. 2019), pp. 22727–22736. DOI: 10.1364/OE.27.022727. URL: https://opg.optica.org/oe/abstract.cfm?URI=oe-27-16-22727.

[33] Manuel Viermetz, Nikolai Gustschin, Clemens Schmid, et al. "Technical Design Considerations of a Human-Scale Talbot-Lau Interferometer for Dark-Field CT". In: *IEEE Transactions on Medical Imaging* 42.1 (2023), pp. 220–232. DOI: 10.1109/TMI.2022.3207579.